Flow structure of the transverse jet interaction with supersonic flow for moderate to high pressure ratios

Asel Beketaeva, Altynshash Naimanova

Abstract**—** The vortex structures behind the transverse jet in a supersonic flow for moderate to high pressure ratios are studied. Numerical simulation is performed using the three-dimensional Favre-averaged Navier–Stokes equations coupled by the turbulence model which are solved by the algorithm based on the high-order non-oscillatory (ENO) scheme. The simulations correctly captured primary vortices: the well-known two counter-rotating vortices, the primary upstream vortex and the secondary upstream vortex, the horseshoe vortex, the pair of vortex in a separation region, and one pair of vortices appeared due to the interaction of the jet passing through the Mach disk, two pairs of vortices formed due to an overflow above the jet. The additional two vortices are found localized near the wall in the region behind the jet.

Keywords**—** Numerical simulation, supersonic flow, perfect gas, boundary layer, Navier-Stokes equations, pressure ratios parameter, shock wave.

I. Introduction

The high-speed jets in the main flow (JIC) have many applications, for example, the efficient mixing of fuel and air is critical for the supersonic combustion. Also as a result of the interaction of the supersonic jet with transverse free flow, the flow changes its orientation downstream, thus can interact with aerodynamic surfaces. This physics phenomena is used in steering of the air vehicles.

The transverse jet in the supersonic flow has been extensively studied both experimentally [1-4] and theoretically [5-23]. In the works of [1-4] generalization of experimental results of the cross injection of sound jets in a supersonic flow is submitted for the various forms of orifices and wide regimes of the jet to cross-flow pressure ratio. The result of these works is the schematic representation of the flow structures. In accordance to this in Fig. 1a the flow physics is illustrated, where the bow shock wave is the curve *(1)*, the separation shock wave - curve *(2)*, the λ - shaped system of shock waves with two triple points corresponding to the exhaust of the significantly underexpanded jet - curve *(3)* and the vortices ahead of the jet are indicated by the curves *(4)* and *(5)*.

The numerical simulation performed in [5-10,12-13,15,19-23] using the Reynolds averaged equations and the two parametric turbulence model such as k-ε, k-ω models have shown some success in understanding the mechanics of the supersonic cross-flows. This approach numerically confirmed the flow structure presented in the experiments [1-4] for low and moderate numbers of the pressure ratio [5-7, 12-13,15,19-20]. For example, Erdema and Kontis [12] proposed the numerical model closed by the κ−ω SST turbulence model for the transverse jet injection into the supersonic flow with jet to free stream pressure ratios from 8.79 to 63.61. It has been revealed that with increase of the jet pressure ratio, cross-flow structures extend further in upstream and downstream directions. Jet penetration is found to be a linear function of momentum flux, and the separation location extends upstream about four times the penetration height.

In [19] the three-dimensional RANS equations and two SST k–ω equations have been solved for explore the influences of the molecular weight(hydrogen and nitrogen) and injector configuration (circular, square, diamond and equilateral triangular) on the mean flow field properties in the transverse injection strategy for the wide range of the jet-to cross flow pressure ratio (from 4.86 to 25.15) The obtained results show that the low pressure ratio can promote the mixing process independently on the injectant species and the injector configuration. Also the large molecular weight of the injectant can improve the mixing process when the pressure ratio is fixed.

A new scheme of the flow field interaction has been also obtained with the large eddy simulation LES and the DNS technique [14,16-18]. This approaches have brought significant contributions toward understanding the evaluation of the supersonic flow interaction. The structures of the cross-flow jet interaction have been identified, where the different types of coherent structures are generated during the mixing process, shock waves and cross-flow vortices have been illustrated in [11,14,16-18] .

This work is supported in part by the Ministry of Education and Science of Republic of Kazakhstan under grant funding of fundamental research in the natural science field («Numerical simulation of spatial turbulent compressible flows with the injection of jets and solid particles», 2018-2020, IRN of the project AP05131555).

A. Beketaeva is with the Al-Farabi Kazakh National University, Almaty, Kazakhstan (corresponding author to provide phone: 8(727)272-00-48; e-mail: azimaras10@gmail.com).

A. Naimanova is with the Institute of Mathematics and Mathematical Modeling, Almaty, Kazakhstan (e-mail: alt_naimanova@yahoo.com).

Kawai and Lele [11] have performed the numerical study of the supersonic flow with the sonic jet injection. They have shown in detail the flow physics of the clockwise and counterclockwise rotating strong longitudinal vortices for the pressure ratio 5.55 and 8.40.

In [14] the DNS approach with an adaptive mesh refinement technique have been used to investigate the Reynolds number effect on the unsteady mixing layer. It has been revealed that the Reynolds number plays an important role in the mixing process.

The supersonic flow with the sonic transverse jet injection for the momentum flux ratio 1.7 has been simulated with the LES approach in [16]. One of the main result here is that the Kelvin-Helmholtz instabilities generated the large scale eddies on the windward side of the jet shear layer, which effect in better mixing of the two fluids.

The main purpose of Khali and Yao research [18] was the validation of the hybrid RANS-LES simulation results with experimental measurements and the exploration of its further capabilities in predicting the mixing flow phenomena. It has been found that the developed shear layer vortices along the interface between the jet and the cross-flow also appeared due to the Kelvin-Helmholtz instability for the pressure ratio from 5.55 to 8.40.

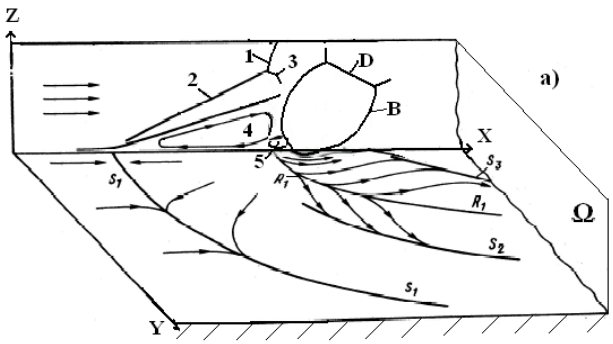

a)

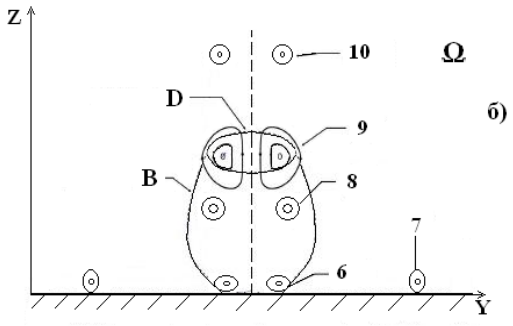

b)

Fig. 1 the jet injection (a) and the vortex pattern (b) in the case of transverse injection of the jet into the freestream.

It is needed to note that the most of numerical simulations of the jet interaction with the cross-flow have been presented for low and moderate values of the pressure ratio(see, e.g. [5-7,12-13,15,19-20]). Although the literature survey shows that the flow physics depends on the wide range of the pressure ratio, which has significant effect on the mixing layer. For example , the presence of the additional vortex structures for the high value pressure ratio has been shown by some authors [9,10,21]. These new vortices was revealed first by [10] for the pressure ratio 282.

These additional vortices are illustrated in Fig. 1b where the vortical structure, located at a certain distance from the jet injection region, entails five pairs of counter-rotating vortices in the cross section *yz* (the plane Ω in Fig. 1a). Two pairs of vortices (*8)* and (*6)* (Fig. 1b) are formed in the mixing region, and one pair of vortices (*9)* is formed due to the interaction of the jet passing through the Mach disk *D* with the high-velocity incoming flow. The horseshoe vortex (*7)* arises if there is the high pressure gradient ahead of the jet as a consequence of the flow separation. Finally, two pairs of vortices (*10)* are formed due to the overflow above the barrel structure *B* in the jet.

Thus, the physical structure of the flow is not fully understood for the wide range value of the pressure ratio which plays key role in the mixing of the jet and main flow. The aim of the present work is the numerical study and detailed analysis of the appearance of new vortical structures for the moderate and high pressure ratios.

II. Physical Models and Numerical Methods

A. Governing Equations

Basic equations for the problem are the system of the three-dimensional Favre averaged Navier-Stokes equations for the compressible turbulent perfect gas in the Cartesian coordinate system written in the conservative form as:

$$\frac{\partial \vec{U}}{\partial t}+\frac{\partial\left(\vec{E}-\vec{E}_v\right)}{\partial x}+\frac{\partial\left(\vec{F}-\vec{F}_v\right)}{\partial y}+\frac{\partial\left(\vec{G}-\vec{G}_v\right)}{\partial z}=S\,, \tag{1}$$

where vectors of dependent variables and vector fluxes are defined by

$$\vec{U}=\left(\rho,\rho u,\rho v,\rho w,E_t,\rho k,\rho\omega\right)^T\,,$$

$$\vec{E}=\left(\rho u,\rho u^2+P,\rho uv,\rho uw,\left(E_t+P\right)u,\rho uk,\rho u\omega\right)^T\,,$$

$$\vec{F}=\left(\rho v,\rho uv,\rho v^2+P,\rho vw,\left(E_t+P\right)v,\rho vk,\rho v\omega\right)^T\,,$$

$$\vec{G}=\left(\rho w,\rho uw,\rho vw,\rho w^2+P,\left(E_t+P\right)w,\rho wk,\rho w\omega\right)^T\,,$$

$$\vec{E}_v=\left(0,\tau_{xx},\tau_{xy},\tau_{xz},u\tau_{xx}+v\tau_{xy}+w\tau_{xz}-q_x,M_k\frac{\partial k}{\partial x},M_\omega\frac{\partial\omega}{\partial x}\right)^T$$

$$\vec{F}_v=\left(0,\tau_{xy},\tau_{yy},\tau_{yz},u\tau_{xy}+v\tau_{yy}+w\tau_{yz}-q_y,M_k\frac{\partial k}{\partial z},M_\omega\frac{\partial\omega}{\partial z}\right)^T$$

$$\vec{G}_v=\left(0,\tau_{xz},\tau_{yz},\tau_{zz},u\tau_{xz}+v\tau_{yz}+w\tau_{zz}-q_z,M_k\frac{\partial k}{\partial y},M_\omega\frac{\partial \omega}{\partial y}\right)^T$$

where $M_k=\frac{1}{\mathrm{Re}}(\mu_l+\sigma_k\mu_t)$, $M_\omega=\frac{1}{\mathrm{Re}}(\mu_l+\sigma_\omega\mu)$.

Components of the viscous stress tensor are given as:

$$\tau_{xx}=\frac{2\mu_t}{3\mathrm{Re}}(2u_x-v_y-w_z),\ \tau_{yy}=\frac{2\mu_t}{3\mathrm{Re}}(2v_y-u_x-w_z),$$
$$\tau_{zz}=\frac{2\mu_t}{3\mathrm{Re}}(2w_z-u_x-v_y),\ \tau_{xy}=\tau_{yx}=\frac{\mu_t}{\mathrm{Re}}(u_y+v_x),$$
$$\tau_{xz}=\tau_{zx}=\frac{\mu_t}{\mathrm{Re}}(u_z+w_x),\ \tau_{yz}=\tau_{zy}=\frac{\mu_t}{\mathrm{Re}}(v_z+w_y).$$

The heat flux is defined by

$$q_x=-\frac{\mu_t}{(\gamma-1)M_\infty^2\mathrm{PrRe}}T_x,\quad q_y=-\frac{\mu_t}{(\gamma-1)M_\infty^2\mathrm{PrRe}}T_y,$$
$$q_z=-\frac{\mu_t}{(\gamma-1)M_\infty^2\mathrm{PrRe}}T_z.$$

The vector of additional terms has the following form:

$$S=\left(0,\ 0,\ 0,0,0,\left(P_k-\beta^*\rho\omega k\right),\left(\gamma^*\rho P_k/\mu_t-\beta\rho\omega^2\right)\right)^T,$$
$$P_k=\mu_t\left[\left(\frac{\partial u_i}{\partial x_j}+\frac{\partial u_j}{\partial x_i}\right)\frac{\partial u_i}{\partial x_j}-\frac{2}{3}\left(\frac{\partial u_k}{\partial x_k}\right)^2\right]-\frac{2}{3}\rho k\frac{\partial u_k}{\partial x_k},\ i,j,k=1,2,3$$
$$\sigma_k=0.5,\sigma_\omega=0.5,\beta^*=0.09,\beta=0.075,\gamma^*=5/9,$$

k,ω are the turbulent kinetic energy and its dissipation rate, P_k is the term defining the turbulence generation, the turbulent viscosity is determined by the formula $\mu_t=\frac{\rho k}{\omega}$ [24], and μ_l is determined by the Sutherland formula.

The pressure and the temperature are given as:

$$P=(\gamma-1)\left[E_t-\frac{1}{2}\left(\rho u^2+\rho w^2+\rho v^2\right)\right],$$
$$T=\left(\frac{1}{\rho c_v}\right)\left[E_t-\frac{1}{2}\left(\rho u^2+\rho w^2+\rho v^2\right)\right],\ c_v=\frac{1}{\gamma(\gamma-1)M_\infty^2}.$$

In the system (1) u,w,v represent the components of the velocity vector, ρ is the density, c_v is the specific heat at constant volume, γ is the ratio of specific heats, M_∞ is the flow Mach number.

The system (1) is written in the nondimensional form. The input parameters of the main flow ($u_\infty,\rho_\infty,T_\infty$) are taken as the governing parameters, the pressure and the total energy are normalized by ($\rho_\infty u_\infty^2$). The injector diameter d is chosen as the characteristic length, Pr is the Prandtl number, and $\mathrm{Re}=u_\infty L/\nu$ is the Reynolds number based on the channel length L.

B. Boundary Conditions

The initial conditions coincide with the boundary conditions at the flowfield entrance.

- at the channel entrance

$$u=1,v=0,w=0,\rho=1,T=1\qquad x=0,0\le y\le H_y,0\le z\le H_z,$$

- on the lower wall,

$$u=0,v=0,w=0,\frac{\partial T}{\partial z}=0,\frac{\partial P}{\partial z}=0\qquad z=0,0<x\le H_x,0\le y\le H_y.$$

At the entrance k,ω are determined using the Baldwin–Lomax algebraic model of turbulence on the base of the known averaged physical parameters of the free stream. Owing to the relation $P_k=\beta^*\rho\omega k$ the initial distribution of the turbulent parameters takes the form:

$$k=k_\infty,\ \text{where}\ k_\infty=\frac{\mu_{tB-L}}{\rho\mathrm{Re}\sqrt{\beta^*}}\sqrt{\frac{P_k}{\mu_{tB-L}}},$$
$$\omega=\omega_\infty,\ \text{where}\ \omega_\infty=\frac{\rho k}{\mu_{tB-L}\mathrm{Re}}.$$

The conditions for k and ω on the wall are

$$k=0,\omega=\frac{6\mu}{0.075\rho(\Delta z_1)^2},$$

here Δz_1 - is the distance from the wall to the first node.

The boundary layer is given near to the wall too, where the longitudinal velocity component in the viscous sublayer [21] is determined by

$$u=0.1\left(\frac{z}{\delta_2}\right)+0.9\left(\frac{z}{\delta_2}\right)^2\qquad x=0,0\le y\le H_y,0\le z\le\delta_2,$$

where $\delta_2=0.1\delta_1$ is the viscous sublayer thickness [25], $\delta_1=0.37x(\mathrm{Re}x)^{-0.2}$ is the boundary layer thickness [26].

In the turbulent boundary layer, the 1/7th power law is used

$$u=\left(\frac{z}{\delta_1}\right)^{1/7}\qquad x=0,0\le y\le H_y,\delta_2<z\le\delta_1.$$

The profile of temperature and density values are taken as [21].

The remaining boundary conditions are imposed in the following manner:

- the conditions at the entrance of the jet are

$$u=0, v=0, T=T_0, w=\sqrt{T_0}\frac{M_0}{M_\infty}, P_0=nP_\infty \quad z=0, \left|x^2+y^2\right|\le R$$

where $n= P_0 / P_\infty$ is the jet pressure ratio and M_0 is the jet Mach number.

The symmetry boundary condition on the upper boundary is specified. The conditions on the side boundaries are the Neumann conditions for all parameters. The NSCBC-like non-reflecting condition is imposed on the output boundary [27]. Here H_x, H_z, and H_y are length, height, and width of the computational domain, respectively, and R is the radius of the circular orifice.

C. Numerical Schemes

Currently the system of Navier-Stokes equations for considered problems are solved with using schemes such as MUSCL, TVD, ENO and WENO (weighted ENO) [7,13,21,28,29]. The main weakness of monotonic and TVD schemes is that in the neighborhood of discontinuities points, their approximation order is reduced to the first one. This leads to the fact that, for example, a TVD scheme of the 5th order of accuracy on smooth monotone solutions for a number of test problems does not exceed the TVD scheme of order 3 in accuracy. The ENO scheme and the WENO finite-difference scheme have a sharp, non-oscillatory solution and the order of approximation is higher than one near discontinuities. The third-order approximation scheme for solving the averaged Navier-Stokes equations based on the ENO scheme has been constructed in [7,13]. The technique has been applied to simulation of the plane supersonic flow with jet injection. In this works it has been shown that the algorithm simulates supersonic flows with jet injection with the sufficient order of the accuracy. To solve this problem, the ENO scheme is generalized to the three-dimensional case. In accordance with this, preliminary in the boundary layer, near the wall and at the level of the jet, in order to more accurately solution for the flow, grid thickening is introduced by means of transformations [13]:

$$\xi=\xi(x), \eta=\eta(z), \zeta=\zeta(y). \tag{2}$$

In this case, the system of equations (1) in generalized coordinates can be written in the form:

$$\frac{\partial \tilde{U}}{\partial t}+\frac{\partial \tilde{E}}{\partial \xi}+\frac{\partial \tilde{F}}{\partial \eta}+\frac{\partial \tilde{G}}{\partial \zeta}=\frac{\partial \tilde{E}_{v2}}{\partial \xi}+\frac{\partial \tilde{E}_{vm}}{\partial \xi}+\frac{\partial \tilde{F}_{v2}}{\partial \eta}+\frac{\partial \tilde{F}_{vm}}{\partial \eta}+\frac{\partial \tilde{G}_{v2}}{\partial \zeta}+\frac{\partial \tilde{G}_{vm}}{\partial \zeta}$$

where $\tilde{U}=\frac{1}{J}\vec{U}$, $\tilde{E}=\left(\frac{\xi_x}{J}\right)\vec{E}$, $\tilde{F}=\left(\frac{\eta_z}{J}\right)\vec{F}$, $\tilde{E}_{v2}=\left(\frac{\xi_x}{J}\right)\vec{E}_{v2}$,

$\tilde{E}_{vm}=\left(\frac{\xi_x}{J}\right)\vec{E}_{vm}$, $\vec{E}_{vm}+\vec{E}_{v2}=\vec{E}_v$, $\vec{E}_{vm}, \vec{E}_{v2}$ - are diffusion terms containing mixed and second derivatives,

$\tilde{F}_{v2}=\left(\frac{\eta_z}{J}\right)\vec{F}_{v2}$, $\tilde{F}_{vm}=\left(\frac{\eta_z}{J}\right)\vec{F}_{vm}$, $\tilde{G}_{v2}=\left(\frac{\zeta_y}{J}\right)\vec{G}_{v2}$,

$\tilde{G}_{vm}=\left(\frac{\zeta_y}{J}\right)\vec{G}_{vm}$, $J=\frac{\partial(\xi,\eta,\zeta)}{\partial(x,z,y)}$ - is the transformation Jacobian.

Following the principle of ENO scheme construction, the initial system of equations is written in the form:

$$\frac{\partial \tilde{U}}{\partial t}+\left(\hat{A}^+ +\hat{A}^-\right)\frac{\partial \vec{E}^m}{\partial \xi}+\left(\hat{B}^+ +\hat{B}^-\right)\frac{\partial \vec{F}^m}{\partial \eta}+\left(\hat{Q}^+ +\hat{Q}^-\right)\frac{\partial \vec{G}^m}{\partial \zeta}-$$
$$\left[\frac{\partial(\tilde{E}_{v2}+\tilde{E}_{vm})}{\partial \xi}+\frac{\partial(\tilde{F}_{v2}+\tilde{F}_{vm})}{\partial \eta}\ \ \frac{\partial(\tilde{G}_{v2}+\tilde{G}_{vm})}{\partial \zeta}\right]=0 \tag{3}$$

where $A=\frac{\partial \vec{E}}{\partial \vec{U}}$, $B=\frac{\partial \vec{F}}{\partial \vec{U}}$, $Q=\frac{\partial \vec{G}}{\partial \vec{U}}$ - are the Jacobian matrices,

$\hat{A}^{\pm}=R\hat{\Lambda}^{\pm}_{\xi}R^{-1}=R\ \frac{1\pm sign(\Lambda_\xi)}{2}\ R^{-1}$, $\vec{E}^m=\tilde{E}+\vec{E}_\xi+\vec{D}_\xi$ - is the modified flux at the nodal points (*i,j.k)*, which consist of the initial convective vectors ($\tilde{E}$) and additional high-order terms ($\vec{E}_\xi, \vec{D}_\xi$).

After factorization of the single-step finite-difference scheme, we obtain the equality for integrating Eq. (3) with respect to time:

$$\left\{I+\Delta t\left[(\hat{A}^+_{i-1/2}\Delta_- A^n_\xi+\hat{A}^-_{i+1/2}\Delta_+ A^n_\xi)+\Delta\tilde{\mu}_\xi\Delta\frac{1}{\tilde{U}_1}\bullet\right]\right\}$$
$$\left\{I+\Delta t\left[(\hat{B}^+_{i-1/2}\Delta_- B^n_\eta+\hat{B}^-_{i+1/2}\Delta_+ B^n_\eta)+\Delta\tilde{\mu}_\eta\Delta\frac{1}{\tilde{U}_1}\bullet\right]\right\}$$
$$\left\{I+\Delta t\left[(\hat{Q}^+_{i-1/2}\Delta_- Q^n_\zeta+\hat{Q}^-_{i+1/2}\Delta_+ Q^n_\zeta)+\Delta\tilde{\mu}_\zeta\Delta\frac{1}{\tilde{U}_1}\right]\right\}\tilde{U}^{n+1}=$$
$$=\tilde{U}^n+\Delta t\left[\frac{\partial \tilde{E}_{v22}{}^n}{\partial \xi}+\frac{\partial \tilde{F}_{v22}{}^n}{\partial \eta}+\frac{\partial \tilde{G}_{v22}{}^n}{\partial \zeta}+\frac{\partial}{\partial \xi}(2\tilde{E}^n_{vm}-\tilde{E}^{n-1}_{vm})+\right.$$
$$\left.+\frac{\partial}{\partial \eta}(2\tilde{F}^n_{vm}-\tilde{F}^{n-1}_{vm})+\frac{\partial}{\partial \zeta}(2\tilde{G}^n_{vm}-\tilde{G}^{n-1}_{vm})\right]-$$
$$-\Delta t\left[\left(\hat{A}^+ +\hat{A}^-\right)\frac{\partial}{\partial \xi}(\vec{E}_\xi+\vec{D}_\xi)\ +\left(\hat{B}^+ +\hat{B}^-\right)\frac{\partial}{\partial \eta}(\vec{E}_\eta+\vec{D}_\eta)+\right.$$

$$+\left(\hat{Q}^{+}+\hat{Q}^{-}\right)\frac{\partial}{\partial\zeta}(\vec{E}_{\zeta}+\vec{D}_{\zeta})\Big]^{n} \qquad (4)$$

where $A_{\xi}=\xi_x A$, $\hat{A}^{+}+\hat{A}^{-}=I$, ($I$ - is the unit matrix),

$\tilde{\mu}_{\xi}=\frac{\mu_t\xi_x^2}{\mathrm{Re}J}$, $\tilde{\mu}_{\eta}=\frac{\mu_t\eta_z^2}{\mathrm{Re}J}$, $\tilde{\mu}_{\zeta}=\frac{\mu_t\zeta_y^2}{\mathrm{Re}J}$.

The central differences of the second order of accuracy have been used for the approximation of the diffusion terms. For the approximation of the terms containing high-order vectors the following expression is used:

$$\left(\hat{A}^{+}+\hat{A}^{-}\right)\frac{\partial}{\partial\xi}(\vec{E}_{\xi}+\vec{D}_{\xi}) = \hat{A}^{-}_{i+1/2\,jk}\left[\left(\vec{E}_{\xi}+\vec{D}_{\xi}\right)_{i+1\,jk}-\left(\vec{E}_{\xi}+\vec{D}_{\xi}\right)_{i\,jk}\right]+$$

$$+\hat{A}^{+}_{i-1/2\,jk}\left[\left(\vec{E}_{\xi}+\vec{D}_{\xi}\right)_{i\,jk}-\left(\vec{E}_{\xi}+\vec{D}_{\xi}\right)_{i-1\,jk}\right]=$$

$$=R\hat{\Lambda}^{-}R^{-1}_{i+1/2\,jk}\Big[\Big(\textbf{\textit{minmod}}\left(\overline{E}_{\xi i+3/2\,jk}\,\overline{E}_{\xi i+1/2\,jk}\right)+$$
$$+\dot{m}\left(\Delta_{-}\hat{D}_{\xi i+3/2\,jk},\Delta_{+}\hat{D}_{\xi i+3/2\,jk}\right)\ if\ \left|\Delta_{-}\tilde{U}_{i+1jk}\right|>\left|\Delta_{+}\tilde{U}_{i+1\,jk}\right|$$
$$+\dot{m}\left(\Delta_{-}\overline{D}_{\xi i+1/2\,jk},\Delta_{+}\overline{D}_{\xi i+1/2\,jk}\right)\ if\ \left|\Delta_{-}\tilde{U}_{i+1jk}\right|\le\left|\Delta_{+}\tilde{U}_{i+1\,jk}\right|\Big)$$
$$-\left(\textbf{\textit{minmod}}\left(\overline{E}_{\xi i+1/2\,jk}\,\overline{E}_{\xi i-1/2\,jk}\right)+\right.$$
$$+\dot{m}\left(\Delta_{-}\hat{D}_{\xi i+1/2\,jk},\Delta_{+}\hat{D}_{\xi i+1/2\,jk}\right)\ if\ \left|\Delta_{-}\tilde{U}_{ijk}\right|>\left|\Delta_{+}\tilde{U}_{ijk}\right|$$
$$\left.+\dot{m}\left(\Delta_{-}\overline{D}_{\xi i-1/2\,jk},\Delta_{+}\overline{D}_{\xi i-1/2\,jk}\right)\ if\ \left|\Delta_{-}\tilde{U}_{ijk}\right|\le\left|\Delta_{+}\tilde{U}_{ijk}\right|\right)\Big]+$$

$$+R\hat{\Lambda}^{+}R^{-1}_{i-1/2\,jk}\Big[\Big(\textbf{\textit{minmod}}\left(\overline{E}_{\xi i+1/2\,jk}\,\overline{E}_{\xi i-1/2\,jk}\right)+$$
$$-\dot{m}\left(\Delta_{-}\hat{D}_{\xi i-1/2\,jk},\Delta_{+}\hat{D}_{\xi i-1/2\,jk}\right)\ if\ \left|\Delta_{-}\tilde{U}_{ijk}\right|\le\left|\Delta_{+}\tilde{U}_{ijk}\right|$$
$$-\dot{m}\left(\Delta_{-}\overline{D}_{\xi i+1/2\,jk},\Delta_{+}\overline{D}_{\xi i+1/2\,jk}\right)\ if\ \left|\Delta_{-}\tilde{U}_{ijk}\right|>\left|\Delta_{+}\tilde{U}_{ijk}\right|\Big)$$
$$-\left(\textbf{\textit{minmod}}\left(\overline{E}_{\xi i-1/2\,jk}\,\overline{E}_{\xi i-3/2\,jk}\right)+\right.$$
$$-\dot{m}\left(\Delta_{-}\hat{D}_{\xi i-3/2\,jk},\Delta_{+}\hat{D}_{\xi i-3/2\,jk}\right)\ if\ \left|\Delta_{-}\tilde{U}_{i\text{-}1jk}\right|\le\left|\Delta_{+}\tilde{U}_{i-1\,jk}\right|+$$
$$\left.-\dot{m}\left(\Delta_{-}\overline{D}_{\xi i-1/2\,jk},\Delta_{+}\overline{D}_{\xi i-1/2\,jk}\right)\ if\ \left|\Delta_{-}\tilde{U}_{i\text{-}1jk}\right|>\left|\Delta_{+}\tilde{U}_{i-1\,jk}\right|\right)\Big]$$

where

$$\overline{E}_{\xi i+1/2}=\left(Rsign(\Lambda)R^{-1}\right)_{i+1/2}\frac{1}{2}\left[I-\frac{\Delta t}{\Delta\xi}\left(R|\Lambda|R^{-1}\right)_{i+1/2}\right]\Delta_{+}\tilde{\tilde{E}}_i,$$

$$\overline{D}_{\xi i+1/2}=\left(Rsign(\Lambda)R^{-1}\right)_{i+1/2}\frac{1}{6}\left[\frac{\Delta t^2}{\Delta\xi^2}\left(R|\Lambda|R^{-1}\right)^2_{i+1/2}-I\right]\Delta_{+}\tilde{\tilde{E}}_i$$

$$\hat{D}_{\xi i+1/2}=\left(Rsign(\Lambda)R^{-1}\right)_{i+1/2}\left[\frac{1}{6}\left(\frac{\Delta t^2}{\Delta\xi^2}\left(R|\Lambda|R^{-1}\right)^2_{i+1/2}-I\right)+\right.$$
$$\left.+\frac{1}{2}\left(I-\frac{\Delta t}{\Delta x}\left(R|\Lambda|R^{-1}\right)_{i+1/2}\right)\right]\Delta_{+}\tilde{\tilde{E}}_i$$

here

$$\textbf{\textit{minmod}}(a,b)=\begin{cases}s\cdot min\left(|a|,|b|\right) & if\quad sign(a)=sign(b)=s\\ 0 & if\quad else\end{cases}$$

$$\dot{m}(a,b)=\begin{cases}a & if\ \ |a|\le|b|\\ b & if\ \ |a|>|b|\end{cases}.$$

System (4) is solved by the method of splitting with respect to the vector $\tilde{U}$ using matrix sweep.

III. Results and Discussion

The calculations are performed on the 251x121x151 staggered grid with the steps over the spatial coordinates. We studied the interaction of the supersonic flow with the $M_{\infty}=4$, $\mathrm{Pr}=0.72$, $\mathrm{Re}=1.87*10^{6}$ parameters with the sonic jet of the perfect gas injected from the orifice with the diameter $d=0{,}476cm$ and the pressure ratio in the range of $10\le n\le100$. The size of the domain is: $H_x=52$ $H_y=32$, $H_z=24$ and the jet center is located at the point with the coordinates $x_0=16$, $y_0=16$. The boundary layer thickness is taken at the entrance $\delta_1=1{,}65$ and the entire boundary layer is resolved with the use of 22-26 nodes. In [21] the applicability of the ENO scheme to solve the problem of the spatial supersonic flow in the channel with injection of perpendicular jets for moderate jet pressure ratio has been demonstrated. On the base of the constructed code Nav3D the detailed analysis of the convergence of the numerical solution is given.

Fig. 2-7 demonstrates the results of the numerical simulation for the pressure ratio n=100. From Fig. 2a it is visible that two oppositely rotating vortices *(4)* and *(5*) are formed ahead the jet for the flows with the high pressure ratio. They appeared as the result of the detachment of the incoming flow caused by the λ- shaped system of the shock waves. This system of the shock waves is illustrated well on the field of the local Mach number and the pressure distribution (Fig. 2b,c). Fig. 2c shows the λ-shaped system of the shock waves (bow, separation and closing shock waves).

The pair of vortices *(8),* generated by the vortex *(5*), as the result of its lateral overflow, is shown in Fig. 3. And, as follows from the numerical experiments, the size of this pair of vortices is increased downstream. For example, the maximum size of the side vortices is observed in the section x=17.61. Apparently, the increase of the size of these vortices is primarily caused by the fact that they are concentrated near to the wall, and enlargement of the boundary layer thickness gives the growth to this pair. While moving downstream it loses its intensity and as the result it's not visible in sections from $x=20.33$ up to $x=21.64$. Such behavior has been obtained in [21] for the flow with the moderate pressure ratio.

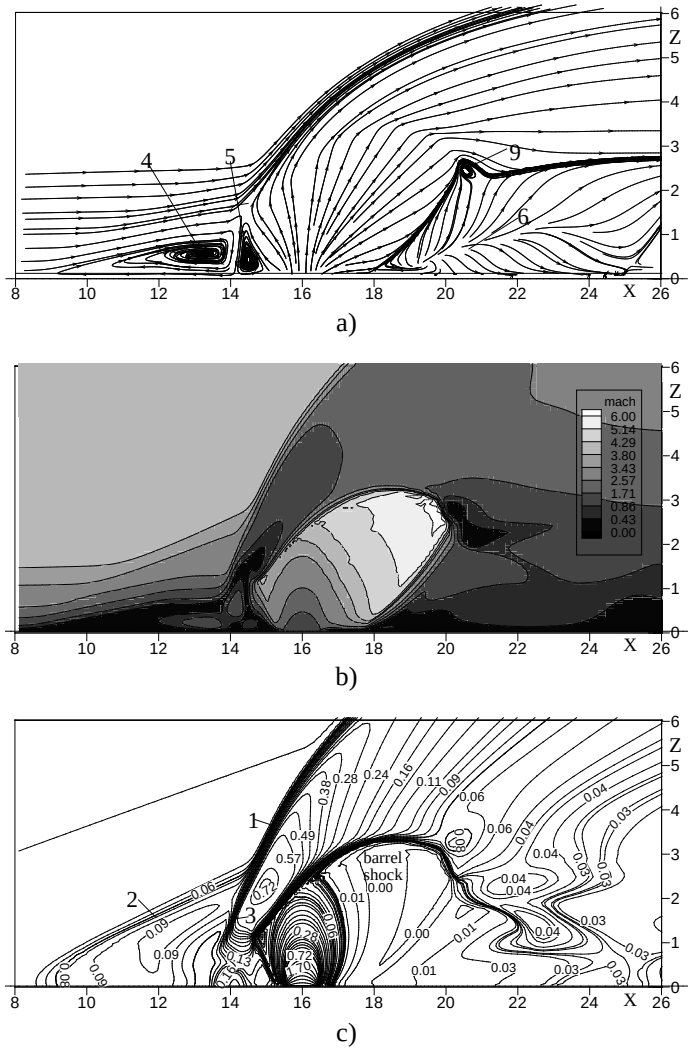

Fig. 2 streamlines (a), mach number (b) and pressure distribution (c) in the plane of symmetry (y=16).

Fig. 4 demonstrates the appearance of the vortex pair *(9)*, which is formed behind the Mach disk due to the interaction of the jet with the rising flow under the jet. Here, the vortex trace *(6)* is also observed near to the wall in the low-pressure region. The presence of these vortex pairs and the mechanisms of their formation have been represented in [21] for the cross-flow with the moderate pressure ratio. Their presence has been shown in [12] for the high ratio too. The numerical experiments reveal that the above-described vortex system is sufficiently stable for the large range regimes of P_0/P_∞.

The reinforced vortex (*8)* is visible in the pair with the vortex *(9)* (Fig. 5 in the section $x = 21.98$). It can be seen from this figure that here, the size of the vortex (*6)* has increased significantly.

Then the vortex *(9)* is captured by the vortex *(8)* (Fig. 6). The vortex *(10)* appears due to the interaction of the jet with the high-velocity flow passing above the injected jet (Fig. 6).

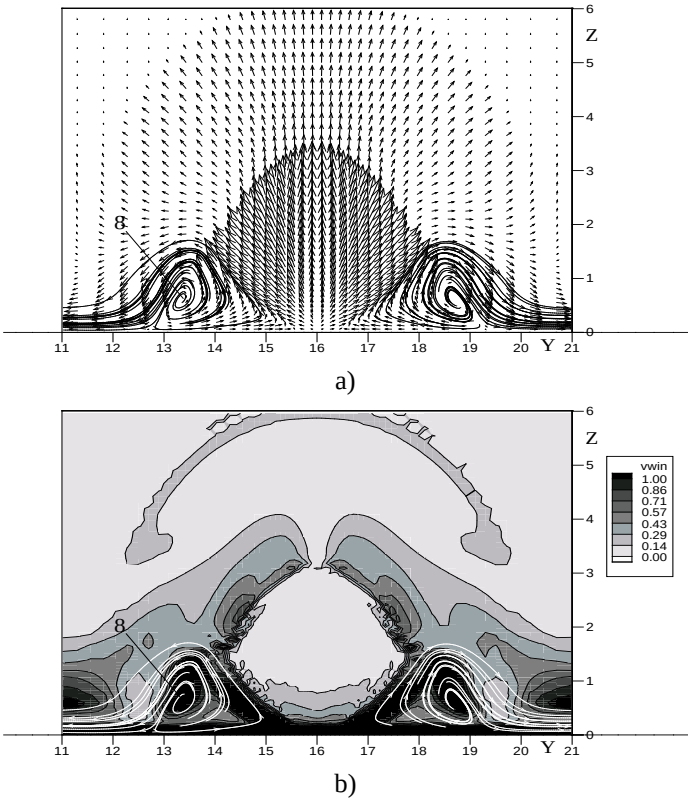

Fig. 3 streamlines (a) and vorticity magnitude (b) in the plane yz (x=17.61)

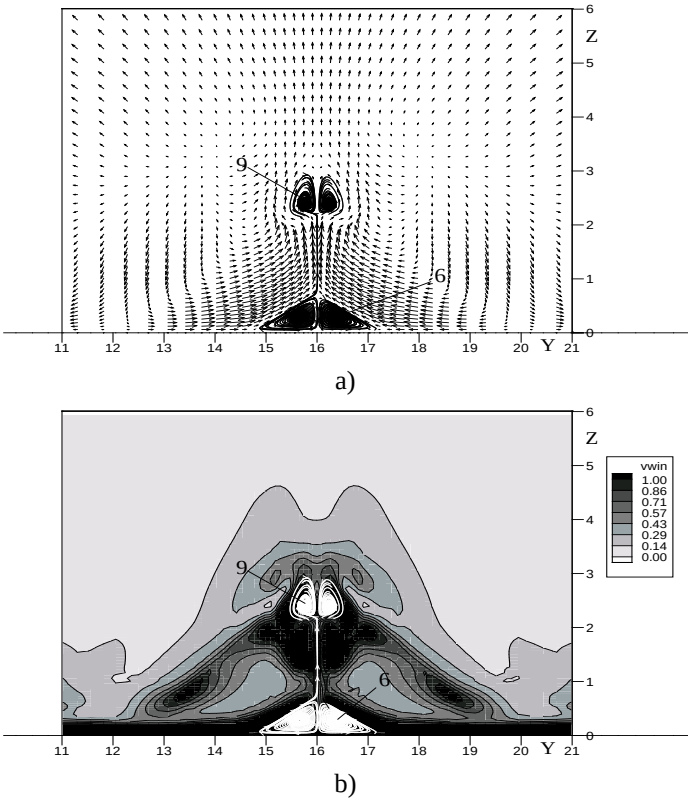

Fig. 4 streamlines (a) and vorticity magnitude (b) in the plane zy (x=21.02)

Then the vortex *(9)* is captured by the vortex *(8)* (Fig. 6). The vortex *(10)* appears due to the interaction of the jet with the high-velocity flow passing above the injected jet (Fig. 6). This vortex has been numerically evidenced firstly in [10] and also in [21].

The pattern of appearance of the vortex *(11)* is also shown in Fig. 6. This vortex formed as the result of the fact that the jet attaches to the surface of the wall [21]. Thus, the assumption that has been put forward in [1] is confirmed here. A namely, between the jet and the region of its attaching to the wall, there is something like a cavity where two counter-rotating vortices may appear. As follows from the Fig.6, the direction of its rotation coincides with the direction of rotation of the track *(6)*.

Fig. 7 shows the vortices *(12)* that are localized near to the wall in the region behind the jet on the distance from the nozzle (at a section $x=18.2$). The physical mechanism of their origin is that the jet, flowing directly from the nozzle, collides with the external flow that tends to get closer to the symmetry line, which leads to the interaction of the counterflows and their twisting in the form of two horns like structures.

The numerical simulation performed for the range of the pressure ratio $10 \leqslant n \leqslant 100$ shows that the behavior of the vortex structure changes with the increase of the parameter n. Thus, at $n=10$, vortices *(6), (8) , (9)* and *(12)* are formed in the region behind the jet, while the vortex structures *(10)* and *(11)* are not been watched, which is possibly caused by that the cross-flow mixing intensity for the smaller pressure ratio is insufficient for the appearance of vortices *(10)* and *(11)*. It is confirmed that starting with parameter $n=20$, these vortices are already identified.

Below, the comparison of the numerical result with the experimental data [1] is performed for the jet to cross-flow with the pressure ratio $n=40$ and the flow parameters $Re=1.87*10^7$, $\Pr=0.9$, $M_\infty=3$, the diameter of the nozzle $d=1.4cm$. Fig. 8 shows the pressure distribution P/P_∞ on the wall in the plane of symmetry (the solid curve shows the computed result and «°°°°» – experimental result [1]). The origin of the chosen coordinate system coincides with the center of the orifice; the abscissa axis shows the values of $X_1=(X-0.5d)-L_1$, where L_1 is the distance from the jet tip to the beginning of the region of the pressure increase. It is seen in Fig. 8 that the braking of the flow ahead of the jet leads to the increase in pressure, and regions with the different pressure gradients are formed. It is also seen in Fig. 8 that numerical and experimental results are in reasonable agreement.

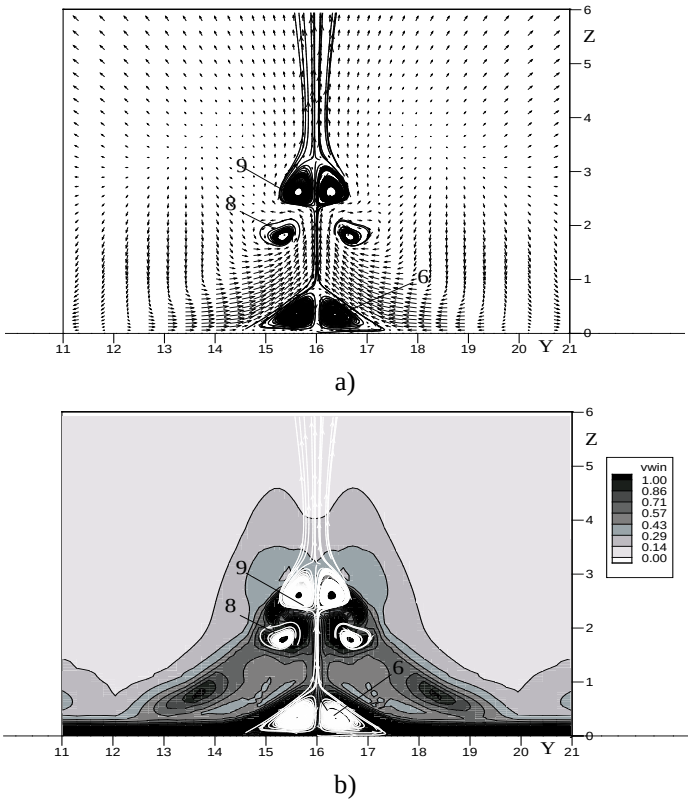

Fig. 5 streamlines (a) and vorticity magnitude (b) in the plane zy (x=21.98)

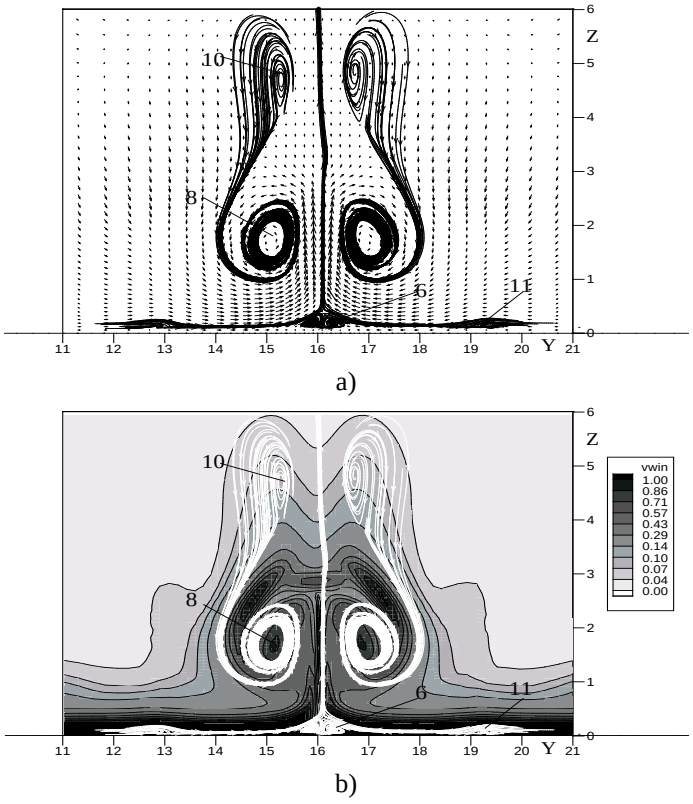

Fig. 6 streamlines (a) and vorticity magnitude (b) in the plane zy (x=29.66)

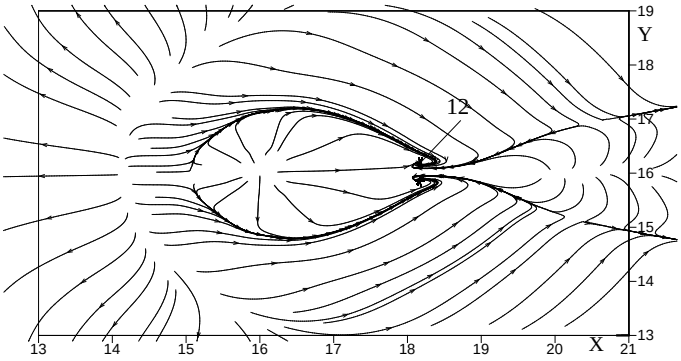

Fig. 7 streamlines in the plane xy (z=0.09)

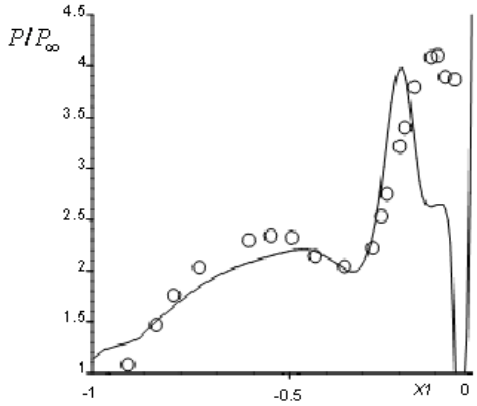

Fig. 8 pressure distribution on the wall on the plane of symmetry

REFERENCES

[1] A. I. Glagolev, A. I. Zubkov, and Yu. A. Panov, "Supersonic Flow around a Gaseous Jet Obstacle on a FlatPlate", *Izv. Akad. Nauk SSSR, Mekh. Zhidk. Gaza*, № 3, pp. 97–102,1967.

[2] F.W. Spaid and E.E. Zukoski, "A Study of the Interaction of Gaseous Jets from Transverse Slots with Supersonic External Flows", *AIAA Journal*, Vol. 6, №. 2, pp. 205−212,1968.

[3] M. R. Gruber, A. S. Nejad, T. H. Chen andJ. C. Dutton, "Transverse injection from circular and elliptic nozzles into a supersonic crossflow", *J. Propulsion and Power*, vol. 16, issue 3, pp. 449-457, 2000.

[4] A. Ben-Yakar, M. G. Mungal and R. K. Hanson, "Time evolution and mixing characteristics of hydrogen and ethylene transverse jets in supersonic crossfows", *Physics of Fluids*, vol. 18, pp. 026101-1-15, 2006

[5] C. F. Chenault and P. S. Beran, "K-ε and Reynolds stress turbulence model comparisons for two-dimensional injection flows", *AIAA J.*,vol. 36, No 8, pp. 1401-1412, 1998.

[6] A.T. Sriram, J. Mathew, "Improved prediction of plane transverse jets in supersonic crossflows", *AIAA Journal*, V.44,№2, pp.405–408, 2006.

[7] A. Beketaeva, A. Naimanova, "Application of ENO (essentially nonoscillatory) scheme to modeling of multi-component flows" *Computational technologies.* V. 12, Special issue 4. pp. 17-25, 2007.

[8] D. A. Dickmann and F.K. Lu, "Shock/Boundary Layer Interaction Effects on Transverse Jets in Crossflow Over a Flat Plate", in *38th Fluid Dynamics Conference and Exhibit*, Seattle, USA, Paper AIAA pp.2008-3723, 2008.

[9] F.K. Lu, D. A. Dickmann, "Topology of supersonic jet interaction flowfields at high pressure ratio" presented at the July 1-4,2008 FLUVISU12-12th French Congress on Visualization in Fluid Mechanics, Nice, France.

[10] V. Viti, R. Neel and J. Schetz, "Detailed flow physics of the supersonic jet interaction flow field", *Physics of Fluids*, vol. 21, pp. 1-16, 2009.

[11] Kawai and S.K. Lele, "Large-Eddy Simulation of Jet Mixing in Supersonic Crossflows", *AIAA Journal*,. Vol. 48, №. 9, pp. 2063−2083,2009.

[12] Erdema and K. Kontis, "Numerical and experimental investigation of transverse injection flows", *Shock Waves*, vol. 20, pp. 103-118, 2010.

[13] P. Bruel and A. Naimanova, "Computation of the normal injection of a hydrogen jet into a supersonic air flow", *Thermophys. and Aeromech.*, vol. 17, № 4, pp. 531-542, 2010.

[14] H. Al-Kuran and M. Ilie, "Reynolds Number Effect on the Turbulent Mixing; Numerical Studies Using DNS with Adaptive Mesh Refinement" presented in 47th AIAA/ASME/SAE/ASEE Joint Propulsion Conference & Exhibit. July 31 − August 03. 2011. San Diego, California.

[15] A.O. Beketaeva, A. Zh. Naimanova, "Numerical study of spatial supersonic flow of a perfect gas with transverse injection of jets", *Journal of applied mechanics and technical physics*, V.52, №6, pp. 896-904, 2011.

[16] Z. A. Rana, B. Thornber, and D. Drikakis, "Transverse jet injection into a supersonic turbulent cross-flow", *Physics of Fluids*, V. **23**, 046103, 2011.

[17] Y. You, H.Luedeke, K. Hannemann, "Injection and mixing in a scramjet combustor: DES and RANS studies", *Proceedings of the Combustion Institute*, V.34, №2, pp. 2083-2092, 2012.

[18] E. H. Khali and Y. Yao, "Mixing flow characteristics for a transverse sonic jet injecting into a supersonic crossflow" In: 53rd AIAA Aerospace Sciences Meeting: AIAA 2015 Sci-Tech Conference, Kissimmee, Florida, USA, 5-9 January 2015. Available from:http://eprints.uwe.ac.uk/24248

[19] Wei Huang, Jun Liu, Liang Jin, Li Yan, "Molecular weight and injector configuration effects on the transverse injection flow field properties in supersonic flows" , *Aerospace Science and Technology*, № 32, pp. 94–102, 2014.

[20] Wei Huang, Jian-guo Tan, Jun Liu, Li Yan "Mixing augmentation induced by the interaction between the oblique shock wave and a sonic hydrogen jet in supersonic flows", *Acta Astronautica*, №117, pp. 142–152, 2015.

[21] A. Beketaeva, P. Bruel and A. Naimanova, "Vortical structures behind a transverse jet in a super-sonic flow at high jet to crossflow pressure ratios", *J. Appl. Mech. and Tech. Phys.*, vol. 56, № 5, pp. 777-788, 2015.

[22] V. Borovoy, I. Egorov, V. Mosharov, V. Radchenko, A. Skuratov and I. Struminskaya "Entropy-layer influence on single-fin and double-fin/boundary-layer interactions", *AIAA J.*, vol. 54, № 2, pp. 443-457, 2016.

[23] Kun Ye, Zhengyin Ye, Jie Wu, Zhan Qu "Effects of plate vibration on the mixing and combustion of transverse hydrogen injection for scramjet", *International journal o f hydrogen energy*, V. 42, pp. 21343-21353, 2017.

[24] D. C. Wilcox, *Turbulence modeling for CFD*. DCW Industries, Inc, USA, pp. 537, 2000.

[25] H. Schlichting, *Boundary-layer theory*. McGraw-Hill, 1979.

[26] L. G. Loytsyanskiy, *Mechanics of liquids and gases*. Pergamon Press, Oxford, 1966.

[27] T.J. Poinsot and S. K. Lele, "Boundary conditions for direct simulation of compressible viscous flows", *J. Comp. Phys.*,V. 101, pp. 104-129, 1992.

[28] A. Harten, S. Osher, B. Engquist, S.R. Chakravarthy, "Some Results on Uniformly High-Order Accurate Essentially Non-Oscillatory Schemes", *Applied Num. Math.*, № 2, pp. 347-377, 1986.

[29] J.Y. Yang, "Third_Order Non-Oscillatory Schemes for the Euler Equations", *AIAA Journal*, V. 29. № 10, pp. 1611-1618, 1991.